



Energy-dependent Analyses of the Gamma-Ray Emission from HESS J1857+026 with Fermi-LAT

Xiaolei Guo , Xi Liu, and Yuliang Xin

School of Physical Science and Technology, Southwest Jiaotong University, Chengdu 610031, People's Republic of China; xlguo@swjtu.edu.cn

Received 2023 October 23; revised 2023 December 14; accepted 2023 December 16; published 2024 January 29

Abstract

We report the discovery of the energy-dependent morphology of the GeV gamma-ray emission from HESS J1857+026 with more than 13 yr of Fermi Large Area Telescope data. The GeV gamma-ray emission from this region is composed of two extended components. The hard component with an index of 1.74 ± 0.07 in the energy range of 0.5–500 GeV is spatially coincident with HESS J1857+026, and its 68% containment radius varies from $\sim 0^\circ.44$ below 40 GeV to $\sim 0^\circ.30$ above 140 GeV. The hard GeV gamma-ray spectrum and the energy-dependent morphology of HESS J1857+026 make it favor a pulsar wind nebula origin, which is associated with the energetic pulsar PSR J1856+0245. The soft component with an index of 2.70 ± 0.16 and another extended gamma-ray source detected in this region, 4FGL J1857.9+0313e, with an index of 2.55 ± 0.07 , are spatially coincident with two molecular clumps in the northeast and southwest of HESS J1857+026, which favors the hadronic process, and the protons could be accelerated by the hypothetical supernova remnant associated with PSR J1856+0245.

Unified Astronomy Thesaurus concepts: [Gamma-ray sources \(633\)](#); [Pulsar wind nebulae \(2215\)](#); [Supernova remnants \(1667\)](#); [Molecular clouds \(1072\)](#); [Gamma-rays \(637\)](#)

1. Introduction

More than 200 very-high-energy (VHE; > 100 GeV) gamma-ray sources have been detected with the operations of ground-based Cherenkov telescopes such as H.E.S.S. (Aharonian et al. 2004), MAGIC (Aleksić et al. 2016), HAWC (Abeysekara et al. 2013), and the Large High Altitude Air Shower Observatory (LHAASO; Cao et al. 2023). The gamma-ray emission could be produced by the hadronic interactions in which π^0 subsequently decays into two gamma-ray photons, or via the inverse Compton (IC) scattering process, or through nonthermal bremsstrahlung radiation from high-energy electrons. Most of the VHE gamma-ray sources have been identified to be pulsar wind nebulae (PWNe), supernova remnants (SNRs), X-ray binaries, TeV halos, and so on. However, some TeV gamma-ray sources are still unidentified, and multiwavelength studies of these sources are crucial for revealing their nature and probing the origin of cosmic rays.

HESS J1857+026 was first discovered as a VHE gamma-ray source with an extension of $(0^\circ.11 \pm 0^\circ.08) \times (0^\circ.08 \pm 0^\circ.03)$ (Aharonian et al. 2008). In H.E.S.S. Collaboration et al. (2018), the morphology of HESS J1857+026 was described by a two-dimensional (2D) Gaussian component with an approximate size of $0^\circ.26 \pm 0^\circ.06$. Hessels et al. (2008) discovered an energetic pulsar, PSR J1856+0245, in the direction of HESS J1857+026, which makes HESS J1857+026 a potential PWN candidate. The period and spin-down luminosity of PSR J1856+0245 are $P = 81$ ms and $\dot{E} = 4.6 \times 10^{36}$ erg s $^{-1}$, respectively, with a characteristic age of $\tau_c = 21$ kyr. The distance of PSR J1856+0245 was first estimated to be ~ 9 kpc, derived by the dispersion measure (DM) with the electron density model

of Cordes & Lazio (2002). An updated distance of ~ 6.3 kpc is given by the ATNF Pulsar Catalog¹ according to the electron density model of Yao et al. (2017).

MAGIC carried out follow-up observations and presented the energy-dependent morphology of this region (MAGIC Collaboration et al. 2014). In the energy range of 300 GeV–1 TeV, the morphology observed by MAGIC is compatible with H.E.S.S. observation. However, two separate gamma-ray sources, named MAGIC J1857.2+0263 (hereafter MAG1) and MAGIC J1857.6+0297 (hereafter MAG2), were detected with the data above 1 TeV. MAG1 is an extended source with an intrinsic extension of $(0^\circ.17 \pm 0^\circ.03_{\text{stat}} \pm 0^\circ.02_{\text{sys}}) \times (0^\circ.06 \pm 0^\circ.03_{\text{stat}} \pm 0^\circ.02_{\text{sys}})$, while MAG2 is compatible with a point source. MAGIC Collaboration et al. (2014) interpreted MAG1 as a PWN powered by PSR J1856+0245, and MAG2 may be associated with a molecular cloud complex containing an H II region located at ~ 3.7 kpc and a possible gas cavity. Another pulsar, PSR J1857+0300, was discovered in the direction of MAG2 (Lyne et al. 2017). The characteristic age and spin-down luminosity of PSR J1857+0300 are $\tau_c \sim 4.6 \times 10^6$ yr and $\dot{E} \sim 2.3 \times 10^{32}$ erg s $^{-1}$, with a distance of ~ 6.7 kpc. Meanwhile, an elliptical superbubble was detected with a neutral gas observation (Petriella et al. 2021), which is also spatially coincident with HESS J1857+026. The kinematical distance of the superbubble is about 5.5 kpc and is close to the DM distance of PSR J1856+0245 (~ 6.3 kpc). Petriella et al. (2021) concluded that the TeV emission of HESS J1857+026 originates from the superbubble, and PSR J1856+0245 is located inside the superbubble. In addition, they found five molecular components in the velocity interval between 78 and 90 km s $^{-1}$ with $^{13}\text{CO}(J = 1-0)$ observations, which are probably associated with the superbubble. And they favor a single gamma-ray source scenario instead of the superposition of two gamma-ray sources. Petriella et al. (2021) also performed radio observations at 1.5 and 6.0 GHz with the Very Large Array (VLA). Nevertheless, no significant radio emission was detected in this region.

Original content from this work may be used under the terms of the [Creative Commons Attribution 4.0 licence](#). Any further distribution of this work must maintain attribution to the author(s) and the title of the work, journal citation and DOI.

¹ <https://www.atnf.csiro.au/research/pulsar/psrcat/>

In the energy range of 1–25 TeV, the Water Cherenkov Detector Array (WCDA) of LHAASO detected an extended gamma-ray source, 1LHAASO J1857+0245, which is spatially consistent with HESS J1857+026 (Cao et al. 2023). The spatial template of 1LHAASO J1857+0245 is described by a 2D Gaussian with $\sigma = 0^\circ.24 \pm 0^\circ.04$, and its gamma-ray spectrum in 1–25 TeV is modeled by a power law with an index of 2.93 ± 0.07 .

The GeV gamma-ray emission from HESS J1857+026 was first detected using a point-source hypothesis by the Fermi Large Area Telescope (LAT; Atwood et al. 2009), while no gamma-ray pulsation from PSR J1856+0245 was observed (Rousseau et al. 2012). Since no obvious X-ray emission was detected, only an upper limit of $F_{1-10 \text{ keV}} = 2 \times 10^{-12} \text{ erg cm}^{-2} \text{ s}^{-1}$ was obtained (Rousseau et al. 2012). Considering the uncertain origin and the complexity of this region, a detailed analysis with more GeV observational data will be helpful to investigate the origin of the gamma-ray emission.

Taking advantage of more than 13 yr of Fermi-LAT data, we performed an energy-dependent analysis of the region around HESS J1857+026 and discussed the nature of this source. The paper is organized as follows. In Section 2, we describe the data analysis routines and present our results. In Section 3, we discuss the radiation mechanisms and the nature of HESS J1857+026. The conclusion of this work is presented in Section 4.

2. Fermi-LAT Data and Results

The Fermi-LAT Pass 8 data we analyzed were collected from 2008 August 4 to 2022 March 4 with energies from 500 MeV to 500 GeV. The region of interest (ROI) is a $10^\circ \times 10^\circ$ square centered at the TeV gamma-ray centroid of HESS J1857+026 (R.A. = $284^\circ.296$, decl. = $2^\circ.667$; H.E.S.S. Collaboration et al. 2018). To reduce the contamination from the Earth limb, events with a zenith angle greater than 90° are eliminated. The standard analysis software *Fermitools*² is used with the instrumental response function P8R3_SOURCE_V3. The models we used to describe the Galactic and isotropic diffuse emissions include *gll_iem_v07.fits*, *iso_P8R3_SOURCE_V3_v1.txt*, and *iso_P8R3_SOURCE_V3_PSF3_v1*.³ In addition, all sources in the incremental version of the fourth Fermi-LAT source catalog (4FGL-DR3; Abdollahi et al. 2020, 2022) within a radius of 15° centered at HESS J1857+026 are included in the model. The binned maximum-likelihood analysis method with *gtlike* is applied. During the fitting procedure, the spectral parameters of all sources located in the ROI are left free, together with the normalizations of the two diffuse backgrounds.

2.1. Spatial Analysis

2.1.1. Average Spatial Extension

In the 4FGL-DR3 catalog, the gamma-ray emission of HESS J1857+026 is described by a uniform disk (named 4FGL J1857.7+0246e) centered at R.A. = $284^\circ.449$, decl. = $2^\circ.774$ with a 68% containment radius of $r_{68} = 0^\circ.50$, which is given by the analysis of Fermi-LAT extended Galactic sources (FGES; Ackermann et al. 2017). Meanwhile, there is a point

source named 4FGL J1857.9+0313c located in the north of the disk, which has no identified counterpart (Abdollahi et al. 2020). In the south of the disk, two point sources named 4FGL J1857.6+0212 and 4FGL J1858.3+0209 are identified to be associated with SNR G35.6-0.4 and HESS J1858+020 (Cui et al. 2021; Zhang et al. 2022). To obtain the spatial template of HESS J1857+026, we performed the spatial extension analysis in the energy ranges of 1–3 GeV (low energy) and 10–500 GeV (high energy), respectively. In the low-energy band, only “PSF3”-type (evclass = 128 and evtype = 32) data with better angular resolution are selected to reduce the contamination from nearby sources, while the data with “SOURCE” type (evclass = 128 and evtype = 3) are used in the high-energy range. After subtracting the background sources included in the model (except for 4FGL J1857.9+0313c in the left panel and 4FGL J1857.7+0246e in the middle and right panels), we created three 2.5×2.5 test statistic (TS) maps centered at HESS J1857+026 with different energy ranges, as shown in Figure 1.

As shown in the left panel of Figure 1, the position of 4FGL J1857.9+0313c given by 4FGL-DR3 is not coincident with the gamma-ray peak of this region. In addition, there are discrepancies between the morphologies of the GeV emission around HESS J1857+026 and the spatial templates given by FGES in both the low- and high-energy bands, as shown in the middle and right panels of Figure 1. Therefore, we refined the spatial templates of HESS J1857+026 of the low (hereafter “Src A”) and high (“Src T”) energies, and the morphology of 4FGL J1857.9+0313c was also reanalyzed. The uniform disk, 2D Gaussian, and H.E.S.S. image model are tested. Meanwhile, a point-source model with the best-fit coordinate calculated by *gtfindsrc* is also applied for Src A and 4FGL J1857.9+0313c to test the spatial extension of it. The MAGIC image above 1 TeV is also adopted as the spatial template of Src T to explore whether or not the gamma-ray emission above 10 GeV is a superposition of two sources, which is similar to MAG1 and MAG2 (MAGIC Collaboration et al. 2014). The centroids and extensions of the 2D Gaussian and uniform disk are fitted by *Fermipy*,⁴ a PYTHON package that automates analyses with the Fermi Science Tools (Wood et al. 2017). The results of the spatial analysis with the different energy ranges are listed in Table 1. From Table 1, we can see that both the uniform disk and 2D Gaussian we analyzed can describe the GeV emission of Src A and 4FGL J1857.9+0313c (hereafter renamed 4FGL J1857.9+0313e). For Src T, a 2D Gaussian model is the best-fit template instead of the MAGIC image, indicating that the GeV emission from Src T is in favor of a one-source scenario instead of two separate gamma-ray sources. In the following analysis, the uniform disk is adopted as the spatial template of Src A and 4FGL J1857.9+0313e, while Src T is described by the 2D Gaussian model.

As shown in the middle panel of Figure 1, the centroid of the gamma-ray emission from Src A is far from the position of PSR J1856+0245/PSR 1857+0300 and is on the edge of the TeV emission of HESS J1857+026, which suggests that there is no spatial coincidence between Src A and the pulsars or TeV emission. For Src T, the extension of the best-fit 2D Gaussian template is much smaller than the result given by FGES, which could be attributable to the improvement of the Galactic diffuse

² <http://fermi.gsfc.nasa.gov/ssc/data/analysis/software/>

³ <http://fermi.gsfc.nasa.gov/ssc/data/access/lat/BackgroundModels.html>

⁴ <https://fermipy.readthedocs.io/en/latest/>

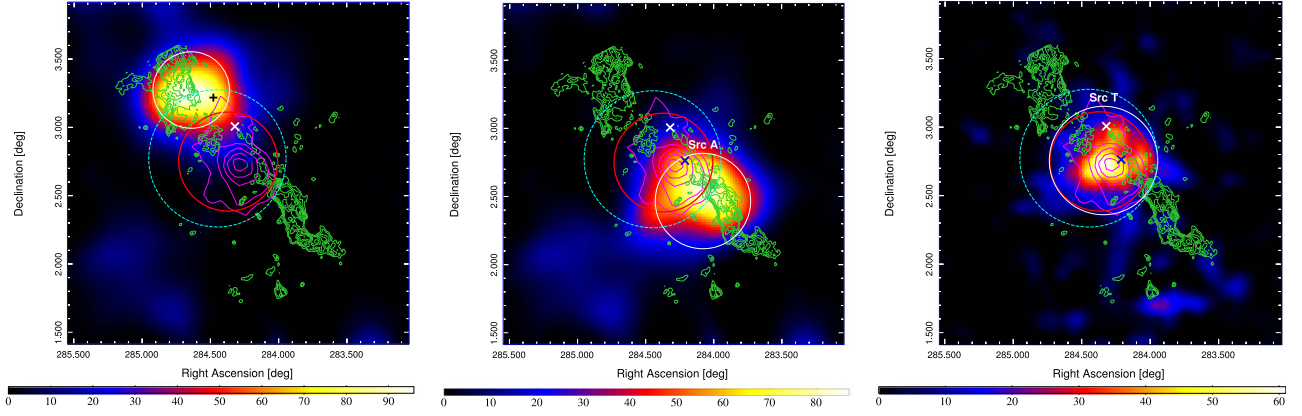


Figure 1. 2.5×2.5 TS maps centered on HESS J1857+026. Each pixel is $0''.02$, and the TS maps are smoothed with a Gaussian kernel of $\sigma = 0''.04$. The green contours indicate the $^{12}\text{CO}(J = 1-0)$ emission integrated between 78 and 90 km s^{-1} by FUGIN (Umemoto et al. 2017). The magenta contours are the H.E.S.S. observation of HESS J1857+026 (H.E.S.S. Collaboration et al. 2018). The cyan dashed circle is the r_{68} of the uniform disk of HESS J1857+026 given by FGES (Ackermann et al. 2017). The red solid circle shows the r_{68} of the 2D Gaussian for 1LHAASO J1857+0245 detected by LHAASO-WCDA (Cao et al. 2023). The blue and white crosses are the positions of PSR J1856+0245 and PSR 1857+0300, respectively. Left: TS map for the data below 3 GeV with the diffuse backgrounds and 4FGL-DR3 sources subtracted, except for 4FGL J1857.9+0313c. The black plus sign shows the position of 4FGL J1857.9+0313c as a point source given by 4FGL-DR3, and the white circle shows the r_{68} of the best-fit uniform disk we analyzed here. Middle: TS map for the data below 3 GeV with the diffuse backgrounds and 4FGL-DR3 sources subtracted, except for Src A. The r_{68} of the uniform disk for Src A is shown by the white circle. Right: TS map with data above 10 GeV. The white circle marks the r_{68} of the best-fit 2D Gaussian model for Src T.

Table 1
Spatial Properties for the GeV Emission in the Direction of HESS J1857+026

Energy Range	Spatial Template	Sources	R.A. (deg)	Decl. (deg)	r_{68}^a (deg)	$\Delta \log L^b$	Degrees of Freedom
1–3 GeV	Point+disk (4FGL)	4FGL J1857.9+0313c	284.478	3.219	...	0	10
		Src A	284.449	2.774	0.50		
	Two points	4FGL J1857.9+0313c	284.665	3.260	...	6	9
		Src A	284.038	2.589	...		
	Point+disk	4FGL J1857.9+0313c	284.665	3.260	...	26	10
		Src A	284.169 ± 0.036	2.504 ± 0.047	0.40 ± 0.03		
	Point+Gaussian	4FGL J1857.9+0313c	284.665	3.260	...	25	10
		Src A	284.178 ± 0.045	2.503 ± 0.064	0.51 ± 0.07		
	Two disks	4FGL J1857.9+0313c	284.641 ± 0.035	3.274 ± 0.039	0.28 ± 0.04	34	11
		Src A	284.079 ± 0.043	2.467 ± 0.041	0.35 ± 0.03		
Disk+Gaussian	4FGL J1857.9+0313c	284.641 ± 0.035	3.274 ± 0.039	0.28 ± 0.04	32	11	
	Src A	284.028 ± 0.046	2.498 ± 0.041	0.31 ± 0.05			
Gaussian+disk	4FGL J1857.9+0313c	284.641 ± 0.039	3.273 ± 0.038	0.29 ± 0.06	34	11	
	Src A	284.079 ± 0.043	2.467 ± 0.041	0.35 ± 0.03			
10–500 GeV	Disk (4FGL)	Src T	284.449	2.774	0.50	0	5
	Disk	Src T	284.361 ± 0.030	2.797 ± 0.029	0.36 ± 0.02	15	5
	Gaussian	Src T	284.341 ± 0.031	2.757 ± 0.035	0.40 ± 0.04	20	5
	H.E.S.S. image	Src T	15	2
	MAGIC image	Src T	14	2

Notes.

^a r_{68} is the 68% containment radius, where $r_{68} = 1.51\sigma$ for the 2D Gaussian model and $r_{68} = 0.82\sigma$ for the uniform disk model (Lande et al. 2012).

^b Calculated with respect to the spatial model used in 4FGL-DR3.

background or the newly detected gamma-ray sources. Considering the comparable extension and the spatial coincidence between Src T and the H.E.S.S. observation (H.E.S.S. Collaboration et al. 2018), we suggest that the GeV emission of Src T has the same origin as the TeV emission. In addition, we found that the spectral index of Src A in the energy range of 1–3 GeV is $\Gamma = 2.50 \pm 0.34$, while the spectral index of Src T for the data above 10 GeV is $\Gamma = 1.84 \pm 0.10$. Considering the distinct GeV spectra and morphologies, the origins of Src A and Src T are probably different. Both Src A and Src T are considered in the following analysis.

2.1.2. Energy-dependent Extension Analysis of Src T

To further explore the energy-dependent behavior of Src T, we performed the extension analysis in the energy ranges of 10–40, 40–140, and 140–500 GeV. For Src T, the 2D Gaussian template is adopted, while the centroid and extension in each energy band are refitted with *Fermipy*. The results with the different energy ranges are listed in Table 2, and the corresponding TS maps are presented in Figure 2.

The energy-dependent analysis shows that the extension of Src T in the energy range of 10–40 GeV is larger than that of higher-energy bands, with r_{68} varying from $0''.44$ below

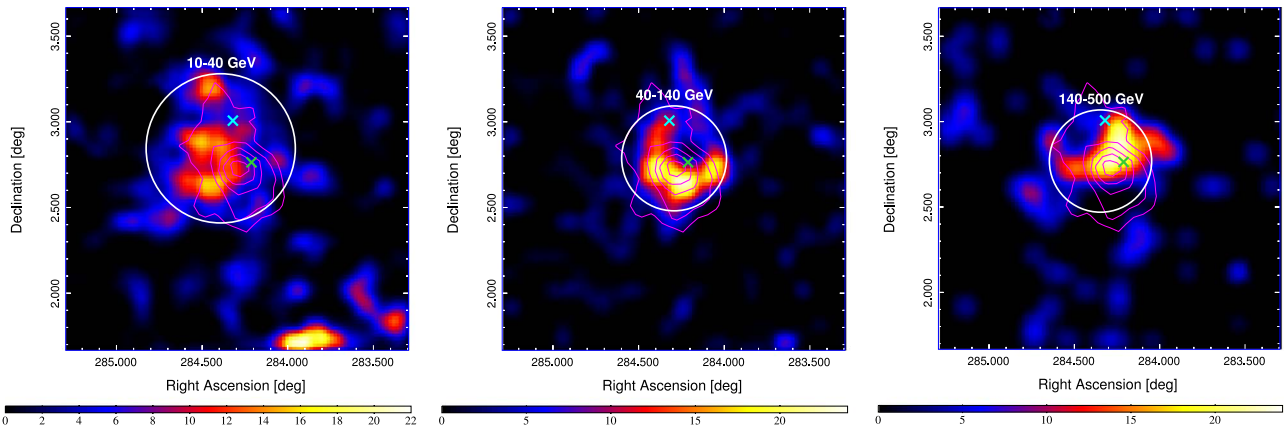


Figure 2. $2^\circ \times 2^\circ$ TS maps centered on HESS J1857+026 in the energy ranges of 10–40 (left), 40–140 (middle), and 140–500 (right) GeV. The white circles indicate the r_{68} of the 2D Gaussian template for the different energy bands. The magenta contours are the H.E.S.S. observation of HESS J1857+026 (H.E.S.S. Collaboration et al. 2018). The positions of PSR J1856+0245 and PSR 1857+0300 are shown as the green and cyan crosses, respectively.

Table 2
Extension Measurements of Src T in the Different Energy Ranges

Energy Range	R.A. (deg)	Decl. (deg)	r_{68} (deg)	TS
10–40 GeV	284.391 ± 0.056	2.846 ± 0.070	0.44 ± 0.07	53
40–140 GeV	284.293 ± 0.049	2.787 ± 0.053	0.31 ± 0.05	52
140–500 GeV	284.347 ± 0.062	2.769 ± 0.059	0.30 ± 0.06	40

40 GeV to $\sim 0^\circ 30'$ above 140 GeV. Similar phenomena are also observed in the typical PWN HESS J1825–137 at TeV and GeV energies (Aharonian et al. 2006; H.E.S.S. Collaboration et al. 2019; Principe et al. 2020). In addition, it should be noted that the gamma-ray emission regions in the energy range of 40–140 and 140–500 GeV seem to be different, as shown in the middle and right panels of Figure 2. However, such phenomena could be attributed to the limited statistics of gamma-ray photons, and more observational data will be helpful to explore the energy-dependent behavior of Src T.

2.2. Spectral Analysis

The spectral analysis was performed in the energy range of 500 MeV–500 GeV. Similar to the spatial analysis, the events of PSF3 type with a better angular resolution were selected for the data below 3 GeV. During the analysis process, the summed likelihood analysis method was adopted, and both Src A and Src T were included in the model with their spatial templates given in Section 2.1.1. The spectra of Src A, Src T, and 4FGL J1857.9+0313e are adopted to be the power-law models. We also tested the GeV spectral curvature for each source by adopting the log-parabola spectrum, while no significant improvement was obtained compared with the power-law models. The global fitting gives a hard spectrum for Src T with a photon index of $\Gamma = 1.74 \pm 0.07$, which is comparable to the result in Rousseau et al. (2012). The integral photon flux is estimated to be $(5.04 \pm 1.08) \times 10^{-9} \text{ ph cm}^{-2} \text{ s}^{-1}$. While the spectrum of Src A is very soft, the photon index is fitted to be $\Gamma = 2.73 \pm 0.10$, with an integral photon flux of $(1.98 \pm 0.19) \times 10^{-8} \text{ ph cm}^{-2} \text{ s}^{-1}$. The best-fit photon index of 4FGL J1857.9+0313e is $\Gamma = 2.55 \pm 0.07$ with an integral photon flux of $(1.41 \pm 0.13) \times 10^{-8} \text{ ph cm}^{-2} \text{ s}^{-1}$.

To study the spectral energy distributions (SEDs) of these three sources, the data are divided into nine logarithmically spaced energy bins. The summed likelihood analysis is

repeated in each energy bin, with only the normalizations of sources located in ROIs and the diffuse backgrounds in the model left free, while the spectral parameters are fixed to be the global fitting values. For the energy bin with a TS value lower than 4.0, an upper limit with a 95% confidence level is calculated. The SEDs are shown in Figure 3. The GeV spectrum of Src T could connect smoothly with the TeV SED of HESS J1857+026, which suggests the same physical origin.

3. Discussion

The spatial and spectral data analyses above reveal that the diffuse GeV gamma-ray emission around HESS J1857+026 could be distinguished into two separate extended components. One of them, namely Src A, has no spatial and spectral coincidence with HESS J1857+026. The other one, namely Src T, shows both spatial and spectral consistency with the TeV measurement of HESS J1857+026, which supports Src T as the GeV counterpart of HESS J1857+026.

Although MAGIC observations revealed two sources in the region of HESS J1857+026, MAGIC1 and MAGIC2, with the events above 1 TeV (MAGIC Collaboration et al. 2014), there is no evidence to show that Src T is composed of two gamma-ray sources limited by the event statistics and the point-spread function of Fermi-LAT. Therefore, we suggest that the GeV emission of HESS J1857+026 originates from a single gamma-ray source. The right panel of Figure 1 shows that the centroid of GeV gamma-ray emission is consistent with PSR J1856+0245 associated with MAGIC1, not PSR J1857+0300 in the direction of MAGIC2, which supports the same origin for HESS J1857+026 and MAGIC1. For the possible origin of the gamma-ray emission from HESS J1857+026, MAGIC Collaboration et al. (2014) suggested a PWN powered by PSR J1856+0245 with $\dot{E} = 4.6 \times 10^{36} \text{ erg s}^{-1}$, and the spin-down luminosity of PSR J1857+0300 with $\dot{E} \sim 2.5 \times 10^{32} \text{ erg s}^{-1}$ is too low to power a gamma-ray PWN (Abdo et al. 2013; Acero et al. 2013). Petriella et al. (2021) revealed the existence of a superbubble with the analysis of atomic gas in this region and suggested a superbubble origin for the TeV emission from HESS J1857+026. However, the hard GeV gamma-ray spectrum of HESS J1857+026 makes it different from the typical superbubble with an index of ~ 2.2 , e.g., Cygnus Cocoon (Ackermann et al. 2011; Aharonian et al. 2019), but is similar to the typical PWNe, e.g., MSH 15–52 (Abdo et al. 2010a)

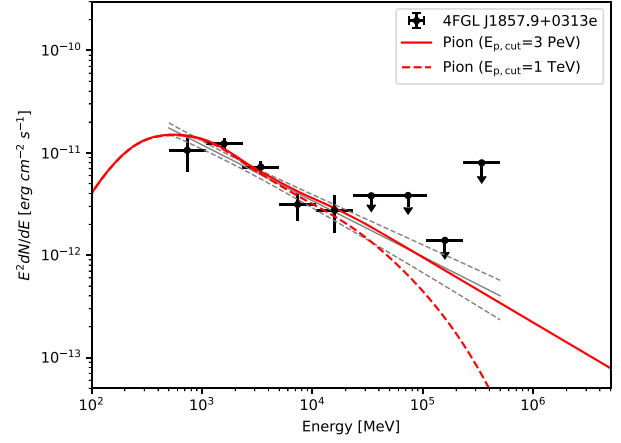
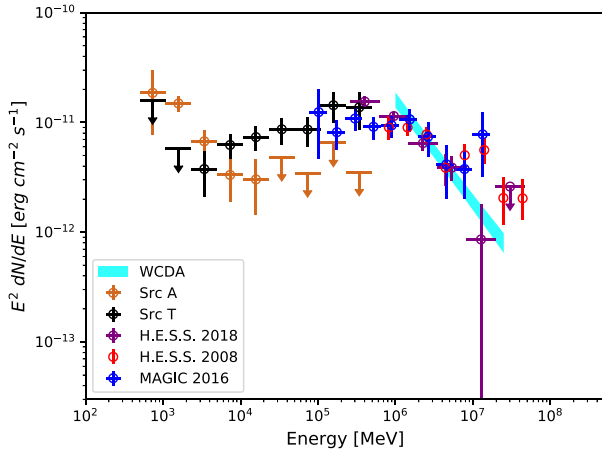


Figure 3. Left: the GeV SEDs of Src A and Src T are marked by the brown and black circles, respectively. The red and purple circles indicate the H.E.S.S. observations by Aharonian et al. (2008) and H.E.S.S. Collaboration et al. (2018), respectively. The blue circles show the MAGIC observation in MAGIC Collaboration et al. (2014). The cyan butterfly indicates the global power-law spectrum of 1LHAASO J1857+0245 detected by LHAASO-WCDA (Cao et al. 2023). Right: the GeV SED of 4FGL J1857.9+0313e. The gray solid and dashed lines show the best-fit power-law spectrum and its 1σ statistic error. The hadronic models with $E_{p,\text{cut}} = 3$ PeV and 1 TeV for 4FGL J1857.9+0313e are shown as the red solid and dashed lines, respectively.

and HESS J1825–137 (Grondin et al. 2011). In addition, the GeV gamma-ray emission of HESS J1857+026 also shows an energy-dependent morphology, with the emission radius varying from $0^\circ.44$ below 40 GeV to $\sim 0^\circ.30$ above 140 GeV. The centroid of the GeV emission moves toward PSR J1856+0245 with increasing energies. Such characteristics are also detected in the PWN HESS J1825–137 and HESS J1303–631 (Aharonian et al. 2006; H.E.S.S. Collaboration et al. 2019, 2012; Principe et al. 2020). All of this evidence supports that the gamma-ray emission of HESS J1857+026 could originate from a PWN associated with PSR J1856+0245.

For PWNe, the emission from radio to X-rays is normally produced by the synchrotron emission, whereas the gamma-ray emission is explained by the IC scattering process (the leptonic process). Here, a simple one-zone leptonic model is applied for HESS J1857+026. The IC background photon fields include the cosmic microwave background and infrared photons from dust with a temperature of $T \sim 30$ K and density of 1 eV cm^{-3} (Rousseau et al. 2012). The distance of HESS J1857+026 is adopted to be 6.3 kpc, derived from the dispersion measurement of PSR J1856+0245 (Yao et al. 2017). Considering the absence of radio detection for the PWN, we used the sensitivity of the VLA in Petriella et al. (2021) to calculate the upper limits of the radio flux by assuming that the spatial extension of the radio PWN is the same as that of the gamma-ray emission with a radius of $0^\circ.4$. The radio upper limits are estimated to be $9.2 \times 10^{-14} \text{ erg cm}^{-2} \text{ s}^{-1}$ at 1.5 GHz and $1.5 \times 10^{-13} \text{ erg cm}^{-2} \text{ s}^{-1}$ at 5 GHz. The electron spectrum is assumed to be a broken power law with an exponential cutoff in the form of $\frac{dN_e}{dE} \propto \frac{(E/E_{\text{br}})^{-\alpha_1}}{1 + (E/E_{\text{br}})^{2-\alpha_1}} \exp\left(-\frac{E}{E_{\text{e,cut}}}\right)$ (Grondin et al. 2011; Xin et al. 2018), where E_{br} , $E_{\text{e,cut}}$, α_1 , and α_2 are the break energy, cutoff energy, and indices of the electron spectrum, respectively. The model fitting is performed using the *naima* package (Zabalza 2015).

As shown in Figure 4, the gamma-ray spectrum of HESS J1857+026 can be reproduced with $\alpha_1 \sim 2.2$ and $\alpha_2 \sim 3.2$, a break energy of $E_{\text{br}} \sim 3.5$ TeV, with a cutoff energy of $E_{\text{e,cut}} \sim 70$ TeV. The total energy of the electrons above 1 GeV, W_e , is calculated to be $\sim 1.1 \times 10^{49} (d/6.3 \text{ kpc})^2 \text{ erg}$. The cooling timescale at the break energy is estimated to be $t_{\text{cool}} \approx 56(E/3.5 \text{ TeV})^{-1}$

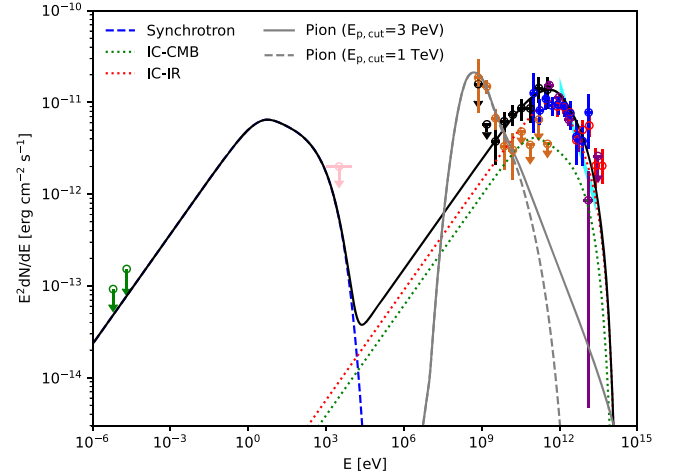


Figure 4. The broadband SED of HESS J1857+026 with the leptonic model and Src A with the hadronic model. The radio and X-ray flux upper limits are shown as the green and pink dots (Rousseau et al. 2012; Petriella et al. 2021). The blue dashed line shows the synchrotron component for HESS J1857+026. The red and green dotted lines represent IC scattering of different seed photons. The black solid line is the sum of different leptonic radiation components for HESS J1857+026. The gray solid and dashed lines indicate the hadronic models with $E_{p,\text{cut}} = 3$ PeV and 1 TeV for Src A.

$[(U_{\text{ph}} + U_{\text{B}})/1.66 \text{ eV cm}^{-3}]^{-1} \text{ kyr}$, where $U_{\text{ph}} = 1.26 \text{ eV cm}^{-3}$ and $U_{\text{B}} = B^2/8\pi$. Such a value is about two times larger than the characteristic age of PSR J1856+0245, which suggests that the break structure could be an intrinsic characteristic of an injected electronic spectrum, not produced by the cooling effect (Gaensler & Slane 2006). With the electron spectrum, the radio and X-ray upper limits constrain the magnetic field strength to be lower than $\sim 4 \mu\text{G}$, which is consistent with the typical values for gamma-ray PWNe (e.g., Grondin et al. 2011, 2013). It should be noted that the X-ray upper limit was calculated with a radius of $0^\circ.1$ by Rousseau et al. (2012). With the same radius of $0^\circ.4$ for the calculation of radio upper limits, the X-ray flux would be much larger, which would have no effect on the SED fitting.

Along with the evolution of the PWN into the interstellar medium (ISM), the energetic electrons could escape from the

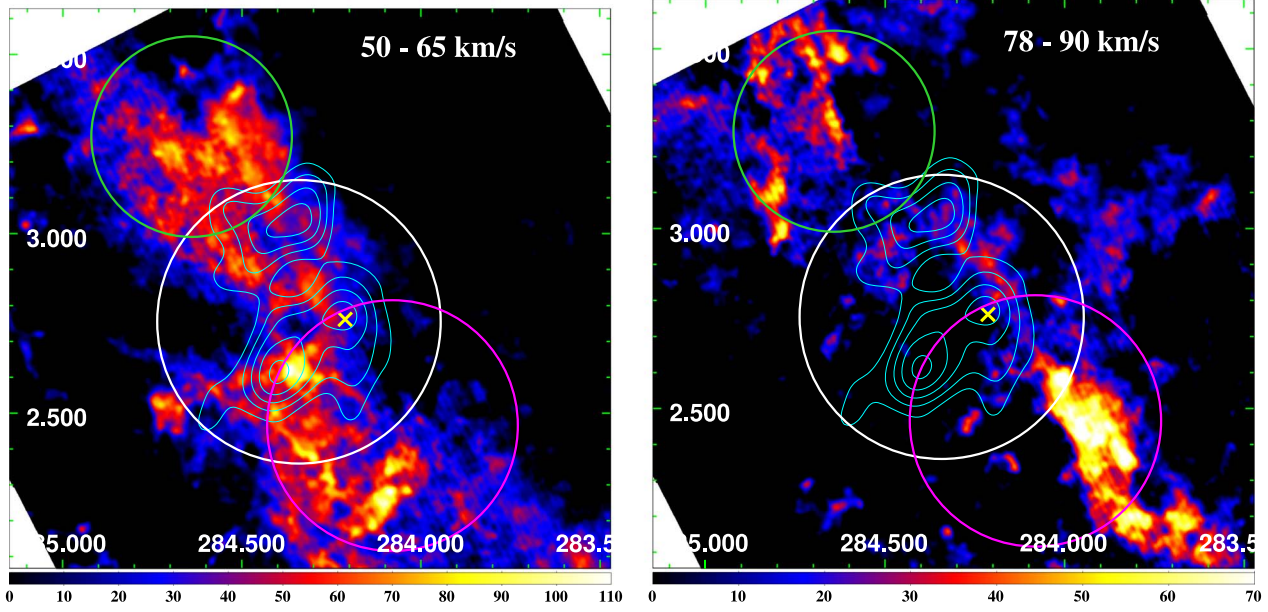


Figure 5. $^{12}\text{CO}(J=1-0)$ intensity maps (in units of K km s^{-1}) in the velocity ranges of 50–65 (left) and 78–90 (right) km s^{-1} . The green, white, and magenta circles show the GeV gamma-ray extensions of Src A, HESS J1857+026, and 4FGL J1857.9+0313e, respectively. The position of PSR J1856+0245 is marked by the yellow cross. The cyan contours indicate the MAGIC gamma-ray flux map above 1 TeV (MAGIC Collaboration et al. 2014).

PWN boundary, and their transport becomes dominated by diffusion, thus potentially forming a detectable halo around the pulsar, which is defined as a pulsar halo. Such halos were first detected around Geminga and PSR B0656+14 with TeV gamma-ray emission (Abeysekara et al. 2017). Di Mauro et al. (2019) also claimed to detect the corresponding GeV gamma-ray emission around Geminga. Based on the definition of an electron halo in Giacinti et al. (2020), namely, the overdensity of relativistic electrons around the pulsar compared with the ISM, we estimate the electronic energy density of HESS J1857+026, ε_e , and compare it with the typical value of the ISM, $\varepsilon_{\text{ISM}} = 0.1 \text{ eV cm}^{-3}$. The gamma-ray emission region of HESS J1857+026 is assumed to be a sphere with a radius of $\sim 0^\circ.40$, which corresponds to a physical radius of $\sim 44 \text{ pc}$ for a distance of 6.3 kpc. Using the total energy of electrons we derived, an electronic energy density of $\varepsilon_e \sim 0.60 \text{ eV cm}^{-3}$ is obtained, which is much larger than that of the ISM. Therefore, we suggest that the relativistic electrons are still contained in a region energetically and dynamically dominated by the pulsar.

Neither of the other two extended gamma-ray sources, Src A and 4FGL J1857.9+0313e, is spatially consistent with the identified counterpart in other wavelengths. By analyzing the $^{12}\text{CO}(J=1-0)$ line data performed by the FOREST Unbiased Galactic plane Imaging survey with the Nobeyama 45 m telescope (FUGIN; Umemoto et al. 2017), two molecular clumps in the southwest (named clump A) and northeast (named clump B) of HESS J1857+026 are founded in the velocity ranges of 50–65 and 78–90 km s^{-1} , as shown in Figure 5, which are spatially coincidence with the GeV gamma-ray emission from Src A and 4FGL J1857.9+0313e, respectively. The molecular clouds in the range of 50–65 km s^{-1} have been revealed in MAGIC Collaboration et al. (2014) with a corresponding kinetic distance of $\sim 3.7 \text{ kpc}$. Petriella et al. (2021) studied the molecular clouds in the range of 79–90 km s^{-1} and derived a kinetic distance of $\sim 5.5 \text{ kpc}$, which is compatible, within the errors, with the DM distance of PSR J1856+0245 ($\sim 6.3 \text{ kpc}$). By adopting the value of the conversion factor of $X_{\text{CO}} = 2 \times 10^{20} \text{ cm}^{-2} (\text{K km s}^{-1})^{-1}$

(Bolatto et al. 2013), we estimate the total mass contents of clumps A and B with the different distances. The total masses of clumps A and B are estimated in the regions of $0^\circ.35$ and $0^\circ.28$ sky integration radii, corresponding to the 68% containment radii of the extended gamma-ray emission of Src A and 4FGL J1857.9+0313e, respectively. For the velocity range of 50–65 km s^{-1} with a distance of 3.7 kpc, the total mass contents of clumps A and B are calculated to be $\sim 2.1 \times 10^5 d_{3.7}^2$ and $\sim 1.7 \times 10^5 d_{3.7}^2 M_\odot$, corresponding to the average gas number densities of $n_{\text{gas,A}} = 175$ and $n_{\text{gas,B}} = 280 \text{ cm}^{-3}$ by assuming a spherical geometry of the gas distribution. For the velocity range of 79–90 km s^{-1} with a compatible distance of PSR J1856+0245 with 6.3 kpc, the total mass contents of clumps A and B are calculated to be $\sim 1.5 \times 10^5 d_{6.3}^2$ and $\sim 1.6 \times 10^5 d_{6.3}^2 M_\odot$, and the corresponding average gas number densities are about $n_{\text{gas,A}} = 27$ and $n_{\text{gas,B}} = 50 \text{ cm}^{-3}$, respectively. The spatial coincidence between the extended gamma-ray emission and the molecular gas suggests a hadronic origin for Src A and 4FGL J1857.9+0313e.

In the hadronic scenario, the proton spectrum is assumed to be a single power law with an exponential cutoff in the form of $\frac{dN_p}{dE} \propto E^{-\gamma} \exp\left(-\frac{E}{E_{p,\text{cut}}}\right)$. The cutoff energy of protons cannot be well constrained and was first adopted to be the energy of the cosmic-ray knee with $E_{p,\text{cut}} = 3 \text{ PeV}$. The hadronic model for Src A is shown as the gray solid line in Figure 4, and the corresponding proton spectrum should be much softer, with $\gamma \sim 2.8$. The total energy of the protons above 1 GeV is estimated to be $W_p \sim 1.6 \times 10^{50} (n_{\text{gas,A}}/27 \text{ cm}^{-3})^{-2} (d/6.3 \text{ kpc})^2$ or $W_p \sim 1.6 \times 10^{48} (n_{\text{gas,A}}/175 \text{ cm}^{-3})^{-2} (d/3.7 \text{ kpc})^2 \text{ erg}$. For 4FGL J1857.9+0313e, the spectral index of protons with $\gamma \sim 2.7$ and total energy of $W_p \sim 5.8 \times 10^{49} (n_{\text{gas,B}}/50 \text{ cm}^{-3})^{-2} (d/6.3 \text{ kpc})^2$ or $W_p \sim 6.4 \times 10^{47} (n_{\text{gas,B}}/280 \text{ cm}^{-3})^{-2} (d/3.7 \text{ kpc})^2 \text{ erg}$ is needed to explain the GeV gamma-ray emission, which is shown as the red solid line in the right panel of Figure 3. In addition, considering the fact that the cutoff energy of protons in the middle-aged SNRs is usually much lower than PeV (Gelfand et al. 2013; Supán et al. 2023), we decreased the cutoff energies of the

protons to estimate the different hadronic models. The allowed minimum value of the cutoff energy is about 1 TeV for Src A and 4FGL J1857.9+0313e, with the total energies of the protons of $\sim 1.5 \times 10^{50} (n_{\text{gas,A}}/27 \text{ cm}^{-3})^{-2} (d/6.3 \text{ kpc})^2$ and $\sim 5.7 \times 10^{49} (n_{\text{gas,B}}/50 \text{ cm}^{-3})^{-2} (d/6.3 \text{ kpc})^2$ erg, respectively.

For the molecular cloud in $50\text{--}65 \text{ km s}^{-1}$ with a distance of 3.7 kpc, there is no candidate for the origin of high-energy protons. For the molecular clouds in $79\text{--}90 \text{ km s}^{-1}$, the compatible distance with PSR J1856+0245 suggests that the hypothetical SNR associated with PSR J1856+0245 could provide enough power, assuming that $\sim 10\%$ of the supernova kinetic energy of $\sim 10^{51}$ erg is transferred to the energy of particles. Moreover, the soft GeV gamma-ray spectra of Src A and 4FGL J1857.9+0313e are also similar to those of the old SNRs interacting with molecular clouds (e.g., IC 443 and W44; Abdo et al. 2010b; Ackermann et al. 2013). The absence of a detection of an associated SNR in this region suggests that it may have already dissipated into the ambient gas. Further observations, especially in the radio and X-ray bands, will be crucial to reveal the physical origin of the gamma-ray emission in this region.

4. Conclusion

Using more than 13 yr of Fermi-LAT observations, we studied the GeV gamma-ray emission in the direction of HESS J1857+026 and found that the GeV emission around HESS J1857+026 is composed of two extended gamma-ray sources: Src A and Src T. Src T is spatially coincident with HESS J1857+026, and its hard GeV gamma-ray spectrum could connect smoothly with the TeV SED of HESS J1857+026, indicating that Src T could be the GeV counterpart of HESS J1857+026. In addition, we performed an energy-dependent analysis of the GeV gamma-ray emission from HESS J1857+026, and its extension decreases toward higher energies. The energy-dependent morphology and the hard GeV gamma-ray spectrum of HESS J1857+026 make it favor a PWN origin. A one-zone leptonic model with a broken power-law electronic spectrum can well describe the multiwavelength data of HESS J1857+026. Src A and another extended gamma-ray source, 4FGL J1857.9+0313e, with soft GeV gamma-ray spectra, have no identified counterparts in other wavelengths. However, two molecular clumps in the northeast and southwest of HESS J1857+026 are spatially coincidence with the GeV gamma-ray emission from Src A and 4FGL J1857.9+0313e, which suggests the hadronic process for their gamma-ray emission. With the single power-law model for protons, the GeV spectra of Src A and 4FGL J1857.9+0313e could also be explained with the soft proton spectra. These high-energy protons could be produced by the hypothetical SNR associated with PSR J1856+0245, which may have already dissipated into the ambient gas.

HESS J1857+026 is one of the peculiar gamma-ray sources that show the energy-dependent morphology. More detailed observations by LHAASO (Cao et al. 2019) and Cherenkov Telescope Array (Cherenkov Telescope Array Consortium et al. 2019) would be helpful to explore the particle transport mechanisms, and future radio and X-ray observations are crucial to investigate the origin of the gamma-ray emission in this region.

Acknowledgments

We acknowledge the use of the Fermi-LAT data provided by the Fermi Science Support Center. This work is supported by the National Natural Science Foundation of China under grants 12103040, 12147208, and U1931204.

ORCID iDs

Xiaolei Guo  <https://orcid.org/0009-0004-5450-8237>
Yuliang Xin  <https://orcid.org/0000-0001-5135-5942>

References

- Abdo, A. A., Ackermann, M., Ajello, M., et al. 2010a, *ApJ*, 714, 927
 Abdo, A. A., Ackermann, M., Ajello, M., et al. 2010b, *Sci*, 327, 1103
 Abdo, A. A., Ajello, M., Allafort, A., et al. 2013, *ApJS*, 208, 17
 Abdollahi, S., Acero, F., Ackermann, M., et al. 2020, *ApJS*, 247, 33
 Abdollahi, S., Acero, F., Baldini, L., et al. 2022, *ApJS*, 260, 53
 Abeyssekara, A. U., Albert, A., Alfaro, R., et al. 2017, *ApJ*, 843, 40
 Abeyssekara, A. U., Alfaro, R., Alvarez, C., et al. 2013, *Aph*, 50, 26
 Acero, F., Ackermann, M., Ajello, M., et al. 2013, *ApJ*, 773, 77
 Ackermann, M., Ajello, M., Allafort, A., et al. 2011, *Sci*, 334, 1103
 Ackermann, M., Ajello, M., Allafort, A., et al. 2013, *Sci*, 339, 807
 Ackermann, M., Ajello, M., Baldini, L., et al. 2017, *ApJ*, 843, 139
 Aharonian, F., Akhperjanian, A. G., Aye, K. M., et al. 2004, *Aph*, 22, 109
 Aharonian, F., Akhperjanian, A. G., Barres de Almeida, U., et al. 2008, *A&A*, 477, 353
 Aharonian, F., Akhperjanian, A. G., Bazer-Bachi, A. R., et al. 2006, *A&A*, 460, 365
 Aharonian, F., Yang, R., & de Oña Wilhelmi, E. 2019, *NatAs*, 3, 561
 Aleksić, J., Ansoldi, S., Antonelli, L. A., et al. 2016, *Aph*, 72, 61
 Atwood, W. B., Abdo, A. A., Ackermann, M., et al. 2009, *ApJ*, 697, 1071
 Bolatto, A. D., Wolfire, M., & Leroy, A. K. 2013, *ARA&A*, 51, 207
 Cao, Z., Aharonian, F., An, Q., et al. 2023, arXiv:2305.17030
 Cao, Z., della Volpe, D., Liu, S., et al. 2019, arXiv:1905.02773
 Cherenkov Telescope Array Consortium, Acharya, B. S., Agudo, I., et al. 2019, Science with the Cherenkov Telescope Array (Singapore: World Scientific)
 Cordes, J. M., & Lazio, T. J. W. 2002, arXiv:astro-ph/0207156
 Cui, Y., Xin, Y., Liu, S., et al. 2021, *A&A*, 646, A114
 Di Mauro, M., Manconi, S., & Donato, F. 2019, *PhRvD*, 100, 123015
 Gaensler, B. M., & Slane, P. O. 2006, *ARA&A*, 44, 17
 Gelfand, J. D., Castro, D., Slane, P. O., et al. 2013, *ApJ*, 777, 148
 Giacinti, G., Mitchell, A. M. W., López-Coto, R., et al. 2020, *A&A*, 636, A113
 Grondin, M. H., Funk, S., Lemoine-Goumard, M., et al. 2011, *ApJ*, 738, 42
 Grondin, M. H., Romani, R. W., Lemoine-Goumard, M., et al. 2013, *ApJ*, 774, 110
 H.E.S.S. Collaboration, Abdalla, H., Abramowski, A., et al. 2018, *A&A*, 612, A1
 H.E.S.S. Collaboration, Abdalla, H., Aharonian, F., et al. 2019, *A&A*, 621, A116
 H.E.S.S. Collaboration, Abramowski, A., Acero, F., et al. 2012, *A&A*, 548, A46
 Hessels, J. W. T., Nice, D. J., Gaensler, B. M., et al. 2008, *ApJL*, 682, L41
 Lande, J., Ackermann, M., Allafort, A., et al. 2012, *ApJ*, 756, 5
 Lyne, A. G., Stappers, B. W., Bogdanov, S., et al. 2017, *ApJ*, 834, 137
 MAGIC Collaboration, Aleksić, J., Ansoldi, S., et al. 2014, *A&A*, 571, A96
 Petriella, A., Duvidovich, L., & Giacani, E. 2021, *A&A*, 652, A142
 Principe, G., Mitchell, A. M. W., Caroff, S., et al. 2020, *A&A*, 640, A76
 Rousseau, R., Grondin, M. H., Van Etten, A., et al. 2012, *A&A*, 544, A3
 Supán, L., Castelletti, G., & Lemièrre, A. 2023, *A&A*, 679, A22
 Umemoto, T., Minamidani, T., Kuno, N., et al. 2017, *PASJ*, 69, 78
 Wood, M., Caputo, R., Charles, E., et al. 2017, *ICRC (Busan)*, 301, 824
 Xin, Y.-L., Liao, N.-H., Guo, X.-L., et al. 2018, *ApJ*, 867, 55
 Yao, J. M., Manchester, R. N., & Wang, N. 2017, *ApJ*, 835, 29
 Zabalza, V. 2015, *ICRC (The Hague)*, 34, 922
 Zhang, X., Chen, Y., Zheng, F.-x., et al. 2022, *ApJ*, 931, 128